ACS APPLIED MATERIALS & INTERFACES

Research Article

www.acsami.org

Role of Associated Defects in Oxygen Ion Conduction and Surface Exchange Reaction for Epitaxial Samaria-Doped Ceria Thin Films as Catalytic Coatings

Nan Yang,[†,‡] Yanuo Shi,[§] Sebastian Schweiger,[§] Evgheni Strelcov,[∥] Alex Belianinov,[∥] Vittorio Foglietti,[†,‡] Pasquale Orgiani,[#,⊥] Giuseppe Balestrino,[†,‡] Sergei V. Kalinin,[∥] Jennifer L. M. Rupp,[§] and Carmela Aruta*[,†]

[†]National Research Council CNR-SPIN and [‡]Department DICII, University of Roma "Tor Vergata" Rome I-00133, Italy

[§]Electrochemical Materials, ETH Zurich, Zurich, 8093, Switzerland

[∥]Center for Nanophase Materials Sciences, Oak Ridge National Laboratory, Oak Ridge, Tennessee 37831, United States

[#]National Research Council CNR-SPIN, University of Salerno, Fisciano, Salerno I-84084, Italy

Supporting Information

ABSTRACT: Samaria-doped ceria (SDC) thin films are particularly important for energy and electronic applications such as microsolid oxide fuel cells, electrolyzers, sensors, and memristors. In this paper, we report a comparative study investigating ionic conductivity and surface reactions for well-grown epitaxial SDC films varying the samaria doping concentration. With increasing doping above 20 mol % of samaria, an enhancement in the defect association is observed by Raman spectroscopy. The role of such associated defects on the films' oxygen ion transport and exchange is investigated by electrochemical impedance spectroscopy and electrochemical strain microscopy (ESM). The measurements reveal that the ionic transport has a sharp maximum in ionic conductivity and drops in its activation energy down to 0.6 eV for 20 mol % doping. Increasing the doping concentration further up to 40 mol %, it raises the activation energy substantially by a factor of 2. We ascribe the sluggish transport kinetics to the "bulk" ionic-near ordering in case of the heavily doped epitaxial films. Analysis of the ESM first-order reversal curve measurements indicates that these associated defects may have a beneficial role by lowering the activation of the oxygen exchange "surface" reaction for heavily doped 40 mol % of samaria. In a model experiment, through a solid solution series of samaria doped ceria epitaxial films, we reveal that the occurrence of associated defects in the bulk affects the surface charging state of the SDC films to increase the exchange rates. The implication of these findings is the design of coatings with tuned oxygen surface exchange by controlling the bulk associated clusters for future electrocatalytic applications.

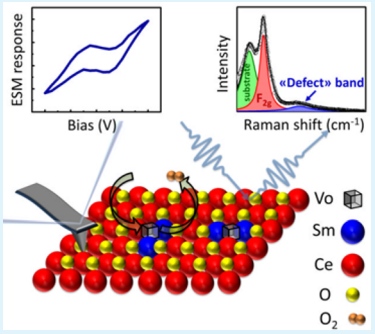

KEYWORDS: *doped ceria, epitaxial thin films, defect associations, Raman, electrochemical strain microscopy*

INTRODUCTION

In the last two decades, pure and doped ceria-based materials attracted a great deal of attention because of their wide range of applications, such as catalysts,[1−3] gas sensors,[4,5] memristors,[6] solar-to-fuel convertors,[7,8] oxygen storage devices,[9] and microsolid oxide fuel cells.[10,11] As a potential catalyst candidate, pure ceria (CeO_2) can adsorb and convert on its surface different chemical species, including H_2, H_2O, CO_x, NO_x, and SO_x in different conditions.[8,12−16] Additionally, it is shown that ceria's catalytic properties may even exceed the performances of some precious metals.[1] The relevance of ceria in catalysis relies on the ability to store and release oxygen in its lattice. This occurs through the generation and annihilation of oxygen vacancies through the $Ce^{4+} \rightarrow Ce^{3+}$ valence change. A significant increase of the oxygen vacancy concentration in the lattice can be achieved by introducing trivalent rare-earth dopants. Among them, samarium is a notable example.[17] The concentration of vacancies is controlled by the neutrality condition, $2[Re'_{Ce}] = [V_o^{\cdot\cdot}]$ in Kroger-Vink notation, where Re'_{Ce} is the rare earth dopant and $V_o^{\cdot\cdot}$ is the formed oxygen vacancy in the lattice. This condition implies that the oxygen vacancy concentration is linearly dependent on the doping level. Indeed, one more vacancy is created every two rare-earth dopant defects introduced into the normal lattice. However, at high doping level, the lattice becomes instable and defect interactions take place. Several types of associated defects can form, as for example, dopant pairs, oxygen-vacancy pairs, dopant ions associated with oxygen vacancies, and Ce^{3+}-based defect pairs, such as $Ce^{3+}-Ce^{3+}$, $Ce^{3+}-$ dopant ions, $Ce^{3+}-$oxygen vacancies.[18−20] Although the increase in the number of vacancies improves the ion conduction, the increase in associated defects amount may have detrimental effects. As a

Received: April 1, 2016
Accepted: May 18, 2016
Published: May 18, 2016

DOI: 10.1021/acsami.6b03909
ACS Appl. Mater. Interfaces 2016, 8, 14613−14621

matter of fact, the conductivity behavior with changing the dopant concentration shows a maximum at 20 mol % for the samaria-doped ceria (SDC), as reported for polycrystalline samples as well.[21,22]

Defect interactions also play a crucial role in the effective ceria surface charge and the oxygen in/decorporation processes, thus affecting the performance of ceria in catalysis. A relevant example is the role of the surface ceria reduction state and its electron localization on the formation of dimer and trimer geometries, as investigated by scanning tunneling microscopy on ceria single crystals.[20] Defect interaction effects have been also invoked to explain the higher reactivity of more negatively charged surface compared to bulk in 20 mol % SDC films, as investigated by in operando X-ray photoelectron spectroscopy (XPS) and electrochemical impedance spectroscopy measurements by Chueh et al.[19] The higher reactivity of the surface was attributed to a higher Ce^{3+} concentration at the surface toward the bulk, which is surprisingly stable even under oxidizing conditions. One hypothesis raised by the authors is that short and long-range ordering may stabilize the surface Ce^{3+} for epitaxially grown samaria-doped ceria films, viz., defect association energies would change. Despite these important first insights, further experimental evidence are mandatory to shed light on the role played by (i) the dopant concentration on the formation of "bulk" associated defects and (ii) their impact on the "surface" oxygen exchange for epitaxial ceria solute solutions.

Recently, we have shown by electrochemical strain microscopy and hard XPS measurements the relevance of the dopant concentration on the mechanisms regulating the oxygen- and/or water-involved reactions in SDC films epitaxially grown on $NdGaO_3$ substrates.[23] The study revealed that by increasing the samaria doping from 10 to 20 mol %, the Ce^{3+} concentration decreased. As a result, the hydrogen evolution reaction worsened in 20 mol % Sm-doped ceria. However, a correlation between the samaria doping and the defect association in stabilizing the Ce^{3+} concentration was not explored. The in operando XPS study of Feng et al.[15] showed that, for undoped ceria, the oxygen incorporation process can be viewed as a series of steps: (1) adsorption of gas molecules onto the surface, (2) oxygen ion/electron transfer across the interface, and (3) oxygen ion diffusion from the surface to the bulk. Cormack and co-workers revealed that the doping level influences the oxygen incorporation process through the vacancy concentration change and/or the diffusion velocity. It was explained in terms of potential defect associations formed between oxygen vacancies and cations based on atomistic computer simulations.[24] First, the increase of the oxygen vacancy concentration is expected to increase the number of active sites for oxygen gas incorporation. Second, a fast diffusion/transport process of oxygen ions can guarantee a continuous supply of oxygen from the bulk to the surface, which promotes surface reactivity. The efficiency of those mechanisms is reduced by increasing the doping level above 20 mol %, when oxygen vacancies become associated with cations. The effect of such cation−vacancy associations, in pure and doped ceria, were studied in terms of transport or surface reactivity.[20,25−27] Some studies suggested that the dopant cation−oxygen vacancy associations modify the activation energy of the thermally activated transport process. This occurs through the change of defect association energies, on the examples of $Ce_{1-x}M_xCeO_2$ (M = Al, Cr, Ga, Fe, Sc, In, Y, Gd, Ce, and La).[25,26] In parallel, other studies on doped ceria pointed out the importance of the Ce^{3+}−oxygen vacancy associations to provide effective adsorption sites for gas molecules.[20,16] In conclusion, a comparative investigation of the role of defect associations induced by the dopant concentration, on both oxygen ion transport and in/decorporation processes, is still missing for epitaxial films (excluding grain boundary effects).

Through this study, the type of the dopant cation is fixed to samarium and its concentration is systematically changed for SDC epitaxial films. Thereby, the size mismatch between hosts and dopant cations is fixed. Samarium is chosen as a dopant because SDC shows the highest conductivity among the plethora of ceria solute solutions.[22] Previously reported studies on epitaxially grown SDC films were focused at the doping concentration value, where the maximum conductivity has been observed, i.e., 20 mol % Sm.[15,19] In this study, we extend the doping concentration as high as 40 mol %. For this, 300 nm epitaxial SDC thin films are grown on $NdGaO_3$ (110) (NGO) substrates by Pulsed Laser Deposition (PLD). We investigate the oxygen in/decorporation processes of epitaxially grown samaria doped ceria thin films with well-defined crystal structure orientation and morphology for various doping levels. We describe the oxygen anionic-cationic bond vibrations changes with respect to samaria doping and epitaxy of these nanometrically flat thin film surfaces turning to Raman microscopy. The changes in the oxygen-cationic bonding environment are discussed in light of association energy variations. Their implications on the transport and the oxygen in/decorporation process are probed by electrochemical impedance spectroscopy (EIS) and electrochemical strain microscopy (ESM). Finally, we conclude on the optimized doping concentration for epitaxially grown samaria-doped ceria films, to increase the surface oxygen exchange for applications as potential catalytic surfaces, i.e., for gas sensing or oxygen capacity-based transfer, or storage surfaces in microelectrochemical devices.

EXPERIMENTAL SECTION

Thin Film Deposition. Pure ceria and SDC epitaxial thin films were grown by PLD on insulating NGO substrates with a thickness of 300 nm. Ceramic stoichiometric targets were prepared in our laboratory starting from commercial 99.99% purity CeO_2 and Sm_2O_3 powders by solid state reaction, then pressing at 200 MPa and sintering at 1500 °C for 5 h. A KrF excimer laser (Coherent Lambda Physik GmbH), with wavelength of 248 nm and pulse width of 25 ns, was focused on the target material in a spot area of about 5 mm^2. The operating frequency was 10 Hz and the energy density 5 J/cm^2. The substrates were ultrasonically cleaned in deionized water, acetone and methanol, and dried with pure nitrogen prior to insertion into the PLD chamber. The deposition was performed at a temperature of about 600 °C, oxygen partial pressure 5 Pa and target-to-substrate distance 3.5 cm. With this set of parameters the deposition rate of about 0.22 Å per laser shot was obtained. The samples were cooled from the deposition temperature down to room temperature at 10 deg min^{-1}.

Thin Electrode Processing. The thin film electrodes were processed by microfabrication. First, the design of electrode was patterned through photolithography (negative photoresist ma-N 1420) by mask aligner (Karl Süss mask aligner MA6). Then 100 nm Pt thin film was deposited by e-beam evaporation (Evaporation Plassys II, deposition rate 1.5 nm/s) because Pt with a high melting temperature will not be influenced by the elevated temperature in the electrochemical measurements. After lift-off process in acetone the microelectrode was fabricated.

X-ray Diffraction Characterization. X-ray diffraction (XRD) analysis was performed on SDC films to determine the structural

DOI: 10.1021/acsami.6b03909
ACS Appl. Mater. Interfaces 2016, 8, 14613−14621

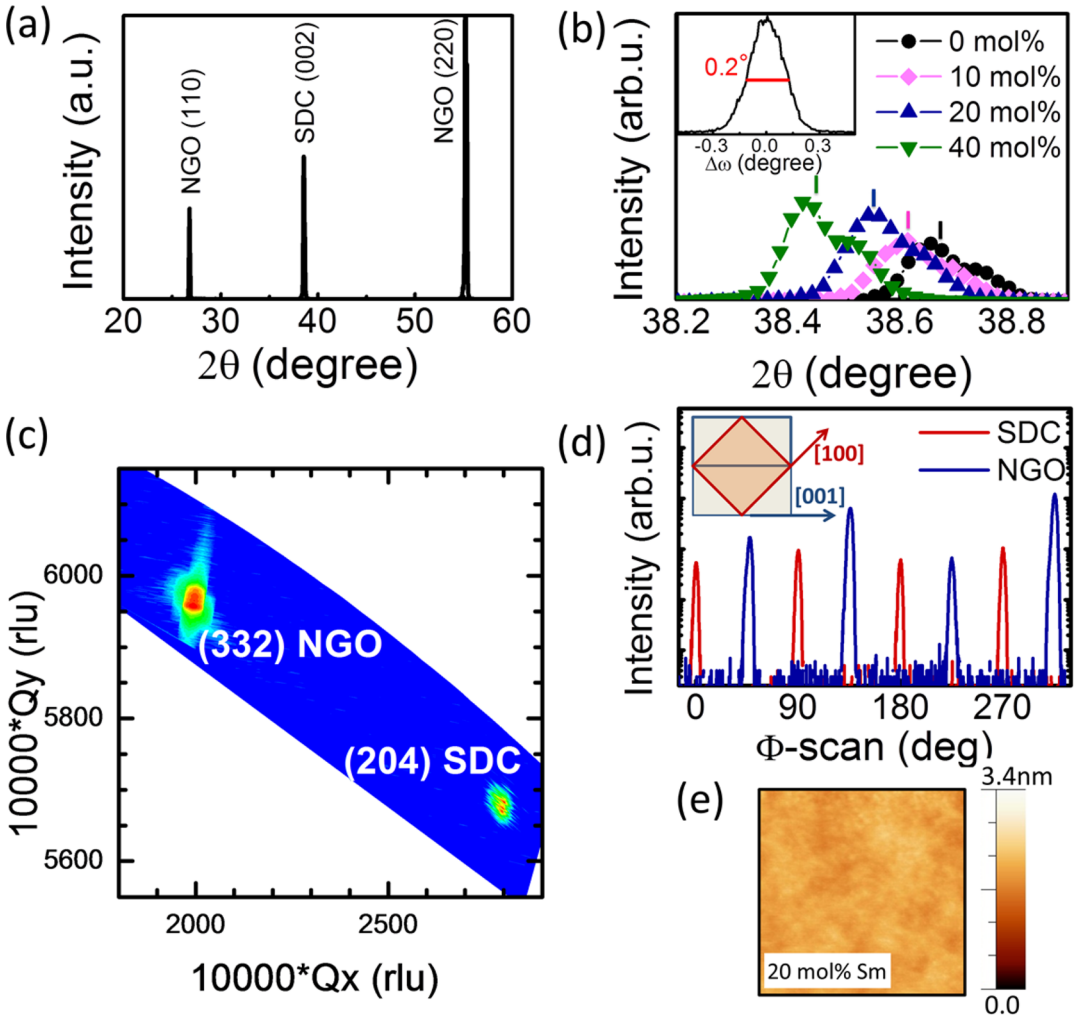

Figure 1. (a) X-ray diffraction $\theta-2\theta$ scan of 20 mol % samaria-doped CeO_2 (SDC) film on $NdGaO_3$(110) (NGO) substrate. b) Enlightened (002) reflection peak behavior of SDC films with different samaria doping from 0 (pure CeO_2) to 40 mol %. The vertical thicks at the maximum peak heights show the Bragg peak shift for the 0 mol % Sm (black), 10 mol % Sm (pink), 20 mol % Sm (blue), and 40 mol % Sm (green) doped films. In the inset the rocking curve of the (002) reflection for the 20 mol % Sm-doped film is also reported. (c) Reciprocal space Qx−Qz map of the (204) of 20 mol % Sm-doped film and the (332) of NGO asymmetric reflections. (d) Azimuthal scans around the same asymmetric reflections and same sample as in panel c. In the inset, the epitaxial relationship sketch obtained from the asymmetric measurements showing the 45° rotation of the two in-plane lattices of film and substrate is shown. (e) AFM topography on a 800 × 800 nm^2 square area of the 20 mol % Sm-doped film.

quality, lattice parameters, to rule out the presence of impurity phases and to determine the epitaxy correlation between the SDC films and the NGO substrate. A Rigaku D-max diffractometer was used in the θ-2θ and rocking curve modes for the symmetric scans using Co Kα radiation, accelerating voltage 30 kV, filament current 30 mA. Reciprocal space maps and azimuthal scans around asymmetric reflections were performed by a Philips X'Pert XRD analytic diffractometer equipped with a four-circle cradle using Cu Kα source, 40 kV and 40 mA.

ESM Spectroscopy. The electrochemical activity of SDC films was investigated in ambient air conditions. The experiments were performed in an ambient commercial atomic force microscope system (Bruker Multimode 8) equipped with a LabVIEW/Matlab based band excitation software for voltage and time spectroscopies. Voltage was applied to a conductive Cr/Pt coated (Budget Sensors) AFM tip, and the bottom electrode was kept grounded. Matlab codes were used for data processing, analysis and fitting.

EIS Analysis. EIS measurements were made with a Gamry FAS2 Femtostat system from 180 to 550 °C in the frequency range from 500 kHz to 0.1 Hz with an AC signal amplitude of 100 mV. The EIS results were analyzed and fitted to the spectra using Z-plot software based on complex nonlinear least-squares fitting method. Details of sample setups including gas feedings and substrate heating were described previously.[28]

Raman Microscopy. Raman microscopy was carried out using a confocal WITec CRM200 Raman microscope instrument (WITec, Germany) equipped with a 532 nm laser for excitation and a 2400g/mm grating, resulting in a spectral resolution better than 0.7 cm^{-1}. To quantify the Raman spectra, we fit all the spectra with Lorentzian peak functions. The component peak numbers and the wavenumber position as well as the full width at half-maximum were fixed for all samples.

RESULTS AND DISCUSSION

SDC thin films with varying dopant concentrations, i.e. $Sm_xCe_{1-x}O_{2-\delta}$ with x = 0, 0.1, 0.2, 0.4, were grown on NGO substrates by PLD. The choice for the upper doping concentration limit at x = 0.4, was made to keep the cubic fluorite structure and to avoid potential formation of the superstructure as seen in higher doping levels.[29]

Figures 1a, b show the XRD $\theta-2\theta$ scan curves in symmetric configuration for the SDC films. The good structural quality is demonstrated by the only presence of the (00l) reflections, with

DOI: 10.1021/acsami.6b03909
ACS Appl. Mater. Interfaces 2016, 8, 14613−14621

a full width at half-maximum (fwhm) of the rocking curve across the (002) reflection about 0.2° (see for instance rocking curve of 20 mol % Sm doping film, reported in inset of Figure 1b). Fwhm values are independent of the doping concentration and are slightly narrower than those reported for previous epitaxial films with 20 mol % Sm doping.[15,30]

The epitaxy correlation between the SDC films and the NGO substrate is obtained by the reciprocal space maps and azimuthal scans in asymmetric configuration, performed across the (332) of NGO and (204) of SDC reflections (as shown in Figure 1c, d for the case of 20 mol % Sm doping). The in-plane 4-fold symmetry of SDC thin films is demonstrated by the azimuthal Φ-scan, measured at the same asymmetric reflections and reported in the Figure 1d, and revealed a rotation of 45° of SDC [100] direction with respect to the NGO [001] direction (as sketched in the inset). XRD reciprocal space map demonstrates the fully in-plane matching condition (within an experimental error of 0.02 Å), between the lattice parameters of SDC thin films and the NGO substrate. These results are a consequence of the very small lattice misfit between the in-plane lattice parameter of SDC and the in-plane diagonal of the NGO substrate, spanning from 0.8 ± 0.2% to 0.1 ± 0.2% for doping variation from pristine to 40 mol % of samaria in ceria, respectively.

However, a progressive elongation of the *c*-axis parameter from 5.41 to5.44 Å with the increasing of samaria concentration is observed as indicated by the 2θ angle shift from 38.65 to 38.43 degrees in Figure 1b. Given that the ionic radius of Sm^{3+} (1.08 Å) is larger than that one of Ce^{4+} (0.97 Å), such an elongation is compatible with a partial substitution of Sm^{3+} ions at Ce^{4+} sites. This result is in a very good agreement with theoretical calculations[31] and previous experimental data on bulk pellets.[32,33] The linear correlation between the *c*-axis parameter and the samaria concentration while keeping the fully in-plane lattice matching between film and substrate, as well as the absence of diffraction peaks related to secondary phases, are compatible with the gradual substitution of Sm atoms at the Ce site without any collapsing of the crystal structure even in the highest doping concentration of 40 mol %. See the Supporting Information for further details.

The topography measurement of the SDC film surface as measured by atomic force microscopy (AFM) is reported in Figure 1e, for the example of the 20 mol % doped ceria film. The samples are nanometrically flat and comparable in their AFM surface topographies for all doping levels, with a root-mean-square surface roughness of about 0.2−0.3 nm. On the basis of XRD and AFM surface analysis, we can conclude that the deposited films are of epitaxial-nature with very smooth surfaces, and therefore they can be treated as model systems with surface/bulk properties only, excluding any grain boundary effects.

Raman spectra of the SDC films excited with a 532 nm laser wavelength measured in ambient are shown in Figure 2a. The Raman spectroscopy allows us to look at the relative change in the samaria doped ceria ionic bond vibrations as a function of its doping concentration, see refs 4, 8, and 34−36 for details. First, we turn to pure CeO_2 film for which one structural main peak is measured in the 400−800 cm^{-1} range. The peak at 465 cm^{-1} is the F_{2g} oxygen anionic−cationic stretching Raman band related to the ceria cubic fluorite structure.[8] It is considered for these structures as the symmetric breathing mode of oxygen ions around each cation with its position depending on the cation−anion bond strength.[10,37] For pure and doped ceria, the

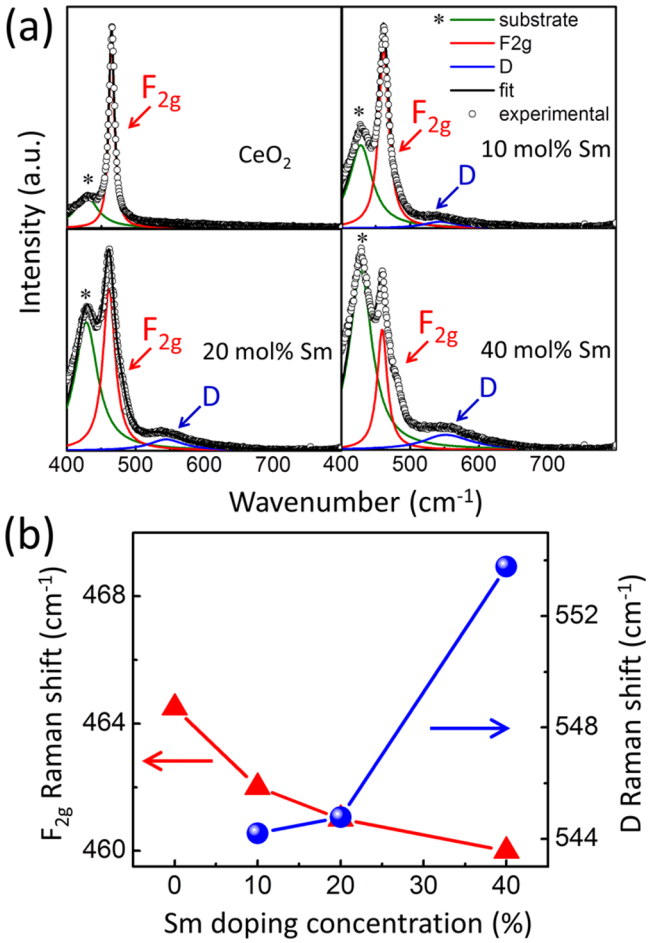

Figure 2. (a) Raman spectra normalized to the maximum peak intensity of samaria doped ceria films with different samaria doping. The peak indicated with star (*) corresponds to the NGO substrate, while the F_{2g} and *D* bands are ascribed to the film. (b) Plot of the Raman shift of F_{2g} and *D* bands as a function of the doping concentration.

decrease (increase) of the wavenumber is associated with the weakening (strengthening) of the bond.[36] We measure that the F_{2g} band shifts systematically to lower wavenumbers, from 465 to 460 cm^{-1} when increasing the doping concentration up to 40 mol %, Figure 2b. This is consistent with the longer cation−anion bond length and consequently weaker cation−anion bond strength, in agreement with the larger lattice parameter detected by XRD and also with earlier Raman literature on doped ceria pellets by McBride[37] and Rupp.[38]

Importantly, doping the epitaxial films with samaria, also results in the uprising of an additional Raman band around 550 cm^{-1} which is denoted as D. In accordance with literature studies,[34,37,39−41] we assign this D Raman band to the second order phonon scattering on oxygen vacancies due to the extrinsic doping with samaria. It is worth noting that although the F_{2g} band shift is almost linear with the dopant concentration, this is not the case for this particular Raman active D band. Here, we observe only a small wavenumber increase of +0.6 cm^{-1} increasing the doping concentration from 10 to 20 mol %, but a very steep wavenumber increase of more than +9.0 cm^{-1} when increasing the doping concentration from 20 to 40 mol %. Such a peculiar D band shift is a direct proof of local environment change around oxygen vacancies.

DOI: 10.1021/acsami.6b03909
ACS Appl. Mater. Interfaces 2016, 8, 14613−14621

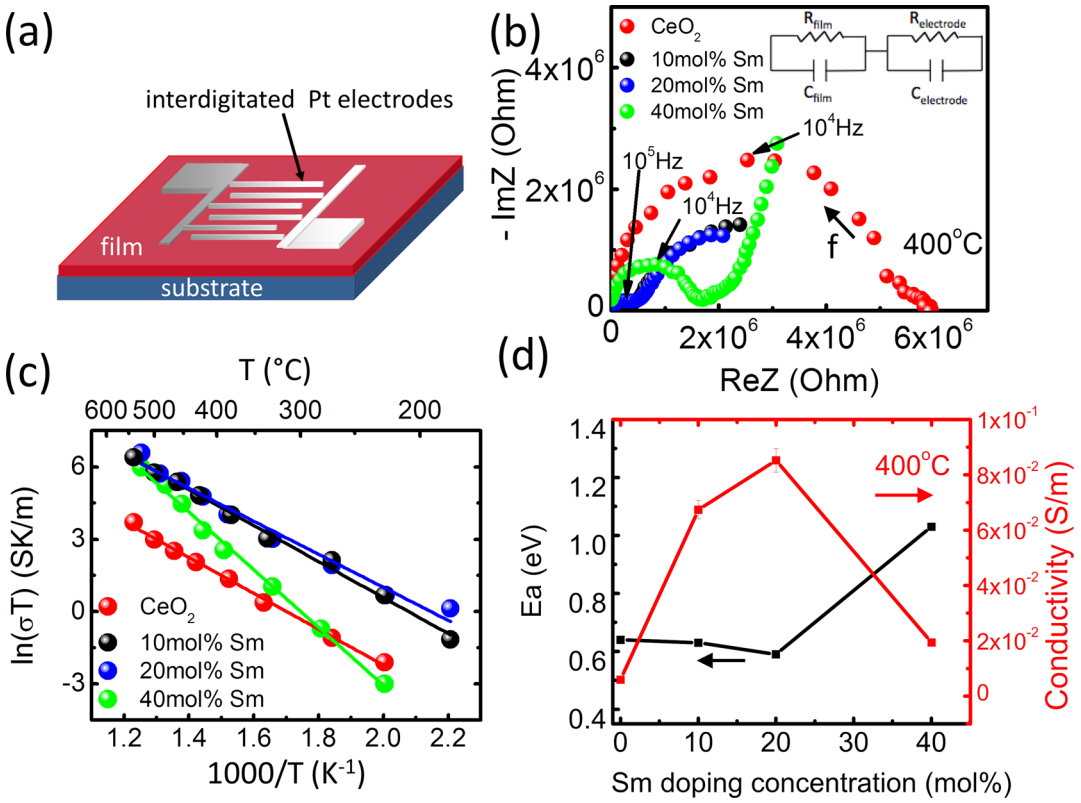

Figure 3. (a) Schematic of measurement electrode setup. (b) Nyquist plots of SDC films at 400 °C in air with the equivalent circuit used to fit the data shown in the inset. (c) Conductivity Arrhenius plot of SDC films involved in this study together with the linear fit. (d) Samaria doping dependence of the activation energy E_a and conductivity at 400 °C.

According to the theoretical and experimental studies on nanoparticles, bulk ceramics and single crystals of doped CeO_2 samples, the shift of the D band at higher wavenumber can be interpreted as changed lattice dynamics due to the increased formation of associated defects, see refs 34 and 39 for details. Taniguchi et al.[34] reported a variation of this second-order phonon scatter D band in a peak intensity increase with doping concentration due to an enhanced defect contribution in gadolinia doped ceria pellets. A slight D band shift was observed, therefore suggesting the formation of a more stable neutral trimer $(2Re'_{Ce}{:}V_O^{\cdot\cdot})^{\times}$ and charged dimer $(2Re'_{Ce}{:}V_O^{\cdot\cdot})^{\bullet}$ complexes in ceria structures. Here, we newly highlight the following defect structural implications based on the measurements on samaria-doped ceria epitaxial films.

First, the occurrence of this associated defect band (second-order phonon scatter band) is most pronounced for heavy doping (i.e., above 20 mol %) with a strong wavenumber shift of +9.0 cm^{-1}. This is a remarkable footprint to measure associated defects via Raman spectroscopy, which we will use to discuss later for oxygen ionic transport measurements in such fluorite structure based oxides.

Second, we report this Raman signature for the case of samaria doping in ceria and can fully ascribe it to the changes in the bulk of the material as no grain boundaries are present in the epitaxial films. Additionally, the observation of Raman vibration modes only associated with the oxygen−cerium−samarium interaction further supports the scenario of continuous Sm substitution at Ce site without any sign of secondary phase segregation.

We now subject the epitaxial samaria-doped ceria films to EIS to study the influence of doping on ionic transport. We use a microfabricated interdigitated Pt electrode geometry as shown in the schematic of Figure 3a to measure the conductivity in air for the temperature range of 180−550 °C. Figure 3b displays the Nyquist plot for the samaria doped ceria films with different doping levels exemplified for 400 °C. The ceria film impedance shows a sole slightly asymmetric semicircle in the Nyquist plot, which is related to the high resistance value of the oxide films, viz., the electrodes are not visible. On the contrary, impedance results on doped ceria films form a semicircle with a tail at lower frequencies, which can be related to the blocking nature of Pt electrodes in the absence of oxygen ion exchange reaction, as demonstrated by measuring the impedance at different DC voltages (see the Supporting Information). The conductivity reported in the Arrhenius type plot of Figure 3c is calculated by using the resistance value obtained by fitting the Nyquist plots to the response of the equivalent circuit shown as an inset in Figure 3b. We employ two RC parallel elements in series to model electrode and film contributions. From the fit of the Arrhenius plot we, in turn, obtain the activation energy (E_a), reported in Figure 3d together with the conductivity at 400 °C, for the case of ceria films with different samaria doping. Further details on the EIS data analysis are reported in the Supporting Information S4.

Analyzing the activation energy conductivity, Figure 3c,d, we measure a clear maximum in transport for 20 mol % Sm doped film and an accordingly lowered activation energy of 0.6 eV for the epitaxial films. This is further in agreement with literature for polycrystalline samaria doped ceria pellets.[21,22] An enhanced doping concentration up to 20 mol % improves the conductivity, thanks to the higher content of induced oxygen vacancies available for the oxygen ion conductivity. On the

DOI: 10.1021/acsami.6b03909
ACS Appl. Mater. Interfaces 2016, 8, 14613−14621

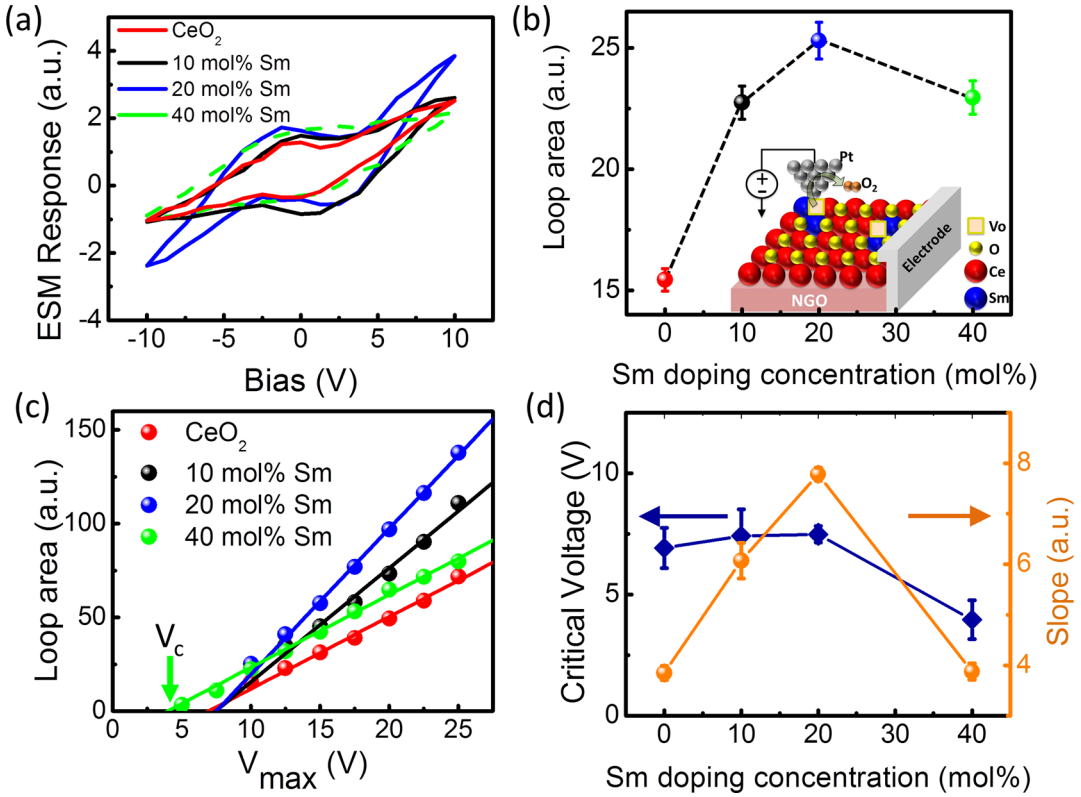

Figure 4. (a) ESM hysteresis loops for the samaria doped CeO_2 films averaged over 1 × 1 μm^2 surface with a 10 × 10 square grid. Loops are all shifted to 0 V for clarity. (b) Areas of the hysteresis ESM loops of panel a as a function of samaria doping. A schematic of the measurement electrode setup is shown in inset. (c) First-order reversal curve (FORC) loop area vs maximum bias voltage (V_{max}). (d) Slope (sphere symbols) and critical voltage V_c (diamond symbols) behavior as a function of the Sm doping concentration obtained by the fit of data reported in panel c.

contrary, further increasing the doping to higher concentrations, the cation-vacancy associated defects start to modify the oxygen ion migration enthalpy, thus affecting the activation energy (E_a) and, thus, the ion conductivity, as measured by EIS.[25]

Interestingly, we measure in the case of the 20 mol % doping a 1 order of magnitude increased conductivity for the epitaxial films (at the order of 1 × 10^{-2} S/m) when compared to polycrystalline bulk pellets (around 1 × 10^{-3} S/m).[21] We ascribe the effect to the higher conduction of bulk in epitaxial case, whereas conventionally processed macrocrystalline pellets may have a blocking grain boundary.[42]

For higher doping concentrations beyond 20 mol %, we measure again an increase in the activation energy, Figure 3d, and drop in the total conductivity for the epitaxially grown samaria doped films. It can be observed that E_a sharply increases up to 1.03 eV for 40 mol % of Sm doping. The obtained E_a values are lower than those reported for polycrystalline samples for the same doping concentrations,[21,22] but quite similar to the reported bulk grain E_a obtained for the polycrystalline samples.[43] According to literature, the increase in E_a for doping concentrations higher than 20 mol % Sm can be attributed to the increase of the association energy between oxygen vacancies and dopant cations forming clusters, see for details refs 21 and 25.

On the basis of the electrochemical impedance measurements in combination with the Raman spectroscopic results, we conclude the following:

First, the epitaxial thin films reveal a clear minimum in activation energy for doping until 20 mol %. This is a bulk driven characteristic. Second, through measuring the oxygen anionic sublattice vibration in the Raman second order vibrations (D Raman shift to higher wavenumber (Figure 2b)), we irrevocably confirm for higher doping concentrations that "oxygen vacancy-samarium dopant clusters" are formed in the epitaxial films, resulting in the increased activation energy of conductivity.

As a next step, we aim at investigating the role of associated defect formation on the oxygen in/decorporation process. The surface kinetics investigation with EIS usually requires the microfabrication of sub 100 nm free-standing membranes. This poses a significant challenge during the preparation process.[44] We apply here a direct nanoscale electrochemical characterization technique, ESM, to probe the surface kinetics of our samples.

ESM measures the surface displacement after application of a short (ms) DC voltage pulse to the tip. In general, for a material with finite ionic conductivity, the associated volume variations are related to the electrochemical processes at the tip−surface junction and ∼20 nm beneath the tip in the oxide.[45] When the tip DC voltage is high enough to overcome both the surface electrochemical reaction overpotential and the potential drop in the material due to the finite conductivity, oxygen vacancies are generated or annihilated by the following oxygen evolution and oxygen reduction reaction (OER/ORR)

$$O_o^{\times} \rightleftharpoons V_o^{\cdot\cdot} + \frac{1}{2}O_2 + 2e^- \quad (1)$$

Oxygen vacancies subsequently diffuse along the concentration gradient and/or drift along in the electric field. The variation in

DOI: 10.1021/acsami.6b03909
ACS Appl. Mater. Interfaces 2016, 8, 14613−14621

the local oxygen vacancy concentration results in a localized strain under the tip, which can be detected through the surface displacement during the DC bias off stage.[45,46]

ESM measurements with the applied voltage of up to 10 V are reported in Figure 4a, b. In Figure 4a, we observe the formation of well-defined ESM hysteresis loops related to the needed finite voltages to activate the forward and reversed redox-processes in the samaria doped ceria films according to eq 1.[46] The schematic of our measurement setup is shown in the inset of Figure 4b. More detailed experimental procedures are described in Supporting Information S2. As can be noted in Figure 4a, the ESM loop shape is similar to a clear signature of activation process onsets when the doping concentration changes. In parallel, the loop area increases when increasing the doping concentration up to 20 mol % and then starts slightly decreasing (Figure 4b).

Because no grain boundary is expected in the films, we can rule out the effects of macroscopic structural defects[47,48] and, thus, we can consider that only the surface reaction and oxygen vacancy motion in the oxide films bulk contribute to these observations. To discriminate between the two effects we use first-order reversal curve (FORC) measurements, a technique detailed in ref 49. Practically, we performed sets of ESM hysteresis measurements at different maximum applied voltages. Assuming that the on-site ion transport process is negligibly affected by the applied DC bias variation in our investigated voltage range, the observed variations in the ESM signal can reasonable be related to the OER/ORR reactions; this is in accordance to earlier observations in ionic oxide systems probed by FORC.[50] The loop area as a function of the maximum DC bias (V_{max}) is shown in Figure 4c. We fit the ESM loop area (LA) dependence on V_{max} with a simple linear function: $\Delta c \propto \mathrm{LA} = A + BV_{max}$, where Δc is the ion concentration variation, the intercept with the x-axis $V_c = -A/B$ is the needed critical voltage for activating the electrochemical surface reaction, and the slope B is related to the ion conductivity inside the sample, see ref 50 for details. Namely, the critical voltage V_c can be considered a key feature for the electrochemical surface reaction, while the slope B gives information on the transport mechanisms. Figure 4d shows that the slope is strongly influenced by the doping level with a maximum at 20 mol %. Because the slope of the FORC data is related to the ion conductivity, this behavior agrees well with the conductivity behavior measured by EIS, even though the FORC measurements are performed at room temperature.

Importantly, the critical voltages are around 7 V independently on the doping concentration for up to 20 mol % of Sm-doping in the epitaxial films (Figure 4d). However, the 40 mol % Sm-doped film reveals a lower critical voltage being <5 V and differs herewith. This leads to the interpretation that a lower potential is needed to effectively activate the OER/ORR reaction at the surface of the heavily doped epitaxial samaria doped ceria film. FORC results suggest that the 40 mol % Sm-doped film donates and accepts electrons in the oxygen in/decorporation reactions more easily at its surface when compared to the films with lower doping content. Chueh et al. explained, on the example of 20 mol % SDC thin films and XPS studies, that high reactivity of entropy-stabilized surfaces can be related to the short-range defect interactions and/or long-range ordering enhanced by the large Ce^{3+} and dopant concentrations.[19] Esch et al. showed that during the surface reaction, electrons left behind by released oxygen localize on cerium ions and favor the formation of associated defects which facilitates the ORR/OER processes in ceria by exposing exclusively Ce^{3+} ions to oxygen gas phase.[20] We propose here that in heavily doped and epitaxial SDC films the lower potential required for the surface reaction process is a consequence of the effective charge of the associated defects present in the bulk. Such an effective charge becomes lower than that of the free oxygen vacancy, thus reducing the effective oxidation state of the oxygen vacancy and increasing its electronegativity. As a matter of fact, the complex defect association favors the electron transfer between the tip and film surface in our ESM experimental configuration and reduces the energy needed for activating the OER/ORR reactions at the tip−surface junction for the 40 mol % Sm-doped film.

We conclude that the presence of associated defects in the 40 mol % Sm, as measured by Raman probing at the given wavelength mostly for the bulk of the film, facilitates the surface charging being beneficial for surface oxygen reaction kinetics of the epitaxial films.

CONCLUSION

In summary, the use of epitaxial thin films with different doping concentration enables new insights into the role of defects in the intrinsic properties of samaria doped ceria materials by eliminating the grain boundary contributions. Raman spectroscopy identifies the increased defect association effects, with increasing of the Sm doping level up to 40 mol % as accessed through analysis of the second order phonon scatter modes. This very Raman mode is a signature for changes in the oxygen sublattice of the bulk oxide film material. Importantly, by using complementary techniques, such as electrochemical strain microscopy and impedance spectroscopy, we show for these heavily doped films the detrimental effects of associated defects on the ion conduction properties and probe surface reactions in the oxygen in/decorporation. As a new insight, we report the observation that even though the bulk of the 40 mol % Sm-doped ceria is characterized by a high formation of associated defects (low oxygen ionic mobility), its surface reveals a higher oxygen exchange activity. This is confirmed by the almost 30% lowered critical voltage for the reaction onset of the heavily doped films, as measured via FORC technique in the electrochemical strain microscopy. Interestingly, our investigation confirms an earlier hypothesis by Chueh et al., predicting the stabilization of doped ceria films at their surfaces by defect interactions in bulk.[19]

Our results show that the intrinsic properties of ceria can be selectively modified by the doping concentration to tune the required functional properties, such as ionic conductivity and oxygen surface reaction rates, on the example of epitaxially grown model solid solutions based on samaria doped ceria films. In particular, the lower electric field necessary for activation of the surface reactions, together with the high-temperature conductivity, propose heavy dopings for the design of ceria based systems for high-temperature electrocatalyst applications for the use in solid oxide fuel cells based on thin films,[10,11] solar energy devices,[7,8] or resistive switching oxides[51,52] operating under high electric fields.

ASSOCIATED CONTENT

Supporting Information

The Supporting Information is available free of charge on the ACS Publications website at DOI: 10.1021/acsami.6b03909.

DOI: 10.1021/acsami.6b03909
ACS Appl. Mater. Interfaces 2016, 8, 14613−14621

Vegard's plot, details on electrochemical strain microscopy, first-order reversal curves, electrochemical impedance spectroscopy (PDF)

AUTHOR INFORMATION

Corresponding Author

*E-mail: carmela.aruta@spin.cnr.it.

Present Address

⊥National Research Council CNR-IOM, TASC National Laboratory, Trieste, I-34149

Funding

Author N.Y. received funding from CNR-Short-term Mobility program 2015. Authors N.Y., P.O., G.B. and C.A. received funding from Italian MIUR FIRB project RBAP115AYN and PRIN project 2010−2011 OXIDE. Authors Y.S., S.S. and J.L.M.R. received funding from Swiss National Science Foundation project numbers 147190, 155986 and 138914.

Notes

The authors declare no competing financial interest.

ACKNOWLEDGMENTS

N.Y. acknowledges CNR-Short Term Mobility program 2015 for the mobility in Switzerland. Italian MIUR is acknowledged for support through the FIRB Project RBAP115AYN "*Oxides at the nanoscale: multifunctionality and applications*" and PRIN Project 2010-2011 OXIDE, "*OXide Interfaces: emerging new properties, multifunctionality, and Devices for Electronics and Energy*". The research at ORNL (ESM measurements) was conducted at the Center for Nanophase Materials Sciences, which is sponsored at Oak Ridge National Laboratory by the Division of Scientific User Facilities, U.S. Department of Energy, supported by project CNMS2014-046 *"Variable temperature and atmosphere local electrochemical characterization of Sm doped CeO_2 epitaxial thin films"*. The research carried out at ETH Zurich was supported by the Swiss National Science Foundation under the project numbers of 147190, 155986, and 138914. C.A., N.Y., and P.O. acknowledge the *"Nanoscience Foundry and Fine Analysis-NFFA"* project through an International Project financed by Italian MIUR.

REFERENCES

(1) Trovarelli, A. Catalytic Properties of Ceria and CeO_2-Containing Materials. *Catal. Rev.: Sci. Eng.* **1996**, *38*, 439−520.

(2) Kaspar, J.; Fornasiero, P.; Graziani, M. Use of CeO_2-Based Oxides in the Three-Way Catalysis. *Catal. Today* **1999**, *50*, 285−298.

(3) Kuhn, M.; Bishop, S. R.; Rupp, J. L. M; Tuller, H. L. Structural Characterization and Oxygen Nonstoichiometry of Ceria-Zirconia ($Ce_{1-x}Zr_xO_{2-\delta}$) Solid Solutions. *Acta Mater.* **2013**, *61*, 4277−4288.

(4) Jasinski, P.; Suzuki, T.; Anderson, H. U. Nanocrystalline Undoped Ceria Oxygen Sensor. *Sens. Actuators, B* **2003**, *95*, 73−77.

(5) Beie, H.-J.; Gnörich, A. Oxygen Gas Sensors Based on CeO_2 Thick and Thin Films. *Sens. Actuators, B* **1991**, *4*, 393−399.

(6) Schweiger, S.; Kubicek, M.; Messerschmitt, F.; Murer, C.; Rupp, J. L. M. A Microdot Multilayer Oxide Device: Let Us Tune the Strain-Ionic Transport Interaction. *ACS Nano* **2014**, *8*, 5032−5048.

(7) Chueh, W. C.; Falter, C.; Abbott, M.; Scipio, D.; Furler, P.; Haile, S. M.; Steinfeld, A. High-Flux Solar-Driven Thermochemical Dissociation of CO_2 and H_2O Using Nonstoichiometric Ceria. *Science* **2010**, *330*, 1797−1801.

(8) Ackermann, S.; Sauvin, L.; Castiglioni, R.; Rupp, J. L. M.; Scheffe, J. R.; Steinfeld, A. Kinetics of CO_2 Reduction Over Nonstoichiometric Ceria. *J. Phys. Chem. C* **2015**, *119*, 16452−16461.

(9) Imtiaz, Q.; Kurlov, A.; Rupp, J. L. M.; Müller, C. R. Highly Efficient Oxygen-Storage Material with Intrinsic Coke Resistance for Chemical Looping Combustion-Based CO_2 Capture. *ChemSusChem* **2015**, *8*, 2055−2065.

(10) Shi, Y.; Bork, A. H.; Schweiger, S.; Rupp, J. L. M. The Effect of Mechanical Twisting on Oxygen Ionic Transport in Solid-State Energy Conversion Membranes. *Nat. Mater.* **2015**, *14*, 721−727.

(11) Evans, A.; Bieberle-Hütter, A.; Rupp, J. L. M.; Gauckler, L. J. Review on Microfabricated Micro-Solid Oxide Fuel Cell Membranes. *J. Power Sources* **2009**, *194*, 119−129.

(12) Shirpour, M.; Gregori, G.; Merkle, R.; Maier, J. On the Proton Conductivity in Pure and Gadolinium Doped Nanocrystalline Cerium Oxide. *Phys. Chem. Chem. Phys.* **2011**, *13*, 937−940.

(13) Kim, S.; Merkle, R.; Maier, J. Water Uptake of Nanocrystalline Ceria: Weight and Conductance Effects. *Solid State Ionics* **2003**, *161*, 113−119.

(14) Feng, Z. A.; Machala, M. L.; Chueh, W. C. Surface Electrochemistry of CO_2 Reduction and CO Oxidation on Sm-Doped CeO_{2-x}: Coupling between Ce^{3+} and Carbonate Adsorbates. *Phys. Chem. Chem. Phys.* **2015**, *17*, 12273−12281.

(15) Feng, Z. A.; El Gabaly, F.; Ye, X.; Shen, Z.-X.; Chueh, W. C. Fast Vacancy-Mediated Oxygen Ion Incorporation Across the Ceria−Gas Electrochemical Interface. *Nat. Commun.* **2014**, *5*, 4374−4382.

(16) Chueh, W. C.; Haile, S. M. A Thermochemical Study of Ceria: Exploiting an Old Material for New Modes of Energy Conversion and CO_2 Mitigation. *Philos. Trans. R. Soc., A* **2010**, *368*, 3269−3294.

(17) Gerhardt-Anderson, R.; Nowick, A. S. Ionic Conductivity of CeO_2 with Trivalent Dopants of Different Ionic Radii. *Solid State Ionics* **1981**, *5*, 547−550.

(18) Grieshammer, S.; Grope, B. O. H.; Koettgen, J.; Martin, M. A Combined DFT + *U* and Monte Carlo Study on Rare Earth Doped Ceria. *Phys. Chem. Chem. Phys.* **2014**, *16*, 9974−9986.

(19) Chueh, W. C.; McDaniel, A. H.; Grass, M. E.; Hao, Y.; Jabeen, N.; Liu, Z.; Haile, S. M.; McCarty, K. F.; Bluhm, H.; El Gabaly, F. Highly Enhanced Concentration and Stability of Reactive Ce^{3+} on Doped CeO_2 Surface Revealed in Operando. *Chem. Mater.* **2012**, *24*, 1876−1882.

(20) Esch, F.; Fabris, S.; Zhou, L.; Montini, T.; Africh, C.; Fornasiero, P.; Comelli, G.; Rosei, R. Electron Localization Determines Defect Formation on Ceria Substrates. *Science* **2005**, *309*, 752−755.

(21) Jung, G.-B.; Huang, T.-J.; Chang, C. − L. Effect of Temperature and Dopant Concentration on the Conductivity of Samaria-Doped Ceria Electrolyte. *J. Solid State Electrochem.* **2002**, *6*, 225−230.

(22) Yahiro, H.; Eguchi, Y.; Eguchi, K.; Arai, H. Oxygen Ion Conductivity of the Ceria-Samarium Oxide System with Fluorite Structure. *J. Appl. Electrochem.* **1988**, *18*, 527−531.

(23) Yang, N.; Belianinov, A.; Strelcov, E.; Tebano, A.; Foglietti, V.; Di Castro, D.; Schlueter, C.; Lee, T.-L; Baddorf, A. P.; Balke, N.; Jesse, S.; Kalinin, S. V.; Balestrino, G.; Aruta, C. Effect of Doping on Surface Reactivity and Conduction Mechanism in Samarium-Doped Ceria Thin Films. *ACS Nano* **2014**, *8*, 12494−12501.

(24) Wang, B.; Lewis, R. J.; Cormack, A. N. Computer Simulations of Large-Scale Defect Clustering and Nanodomain Structure in Gadolinia-Doped Ceria. *Acta Mater.* **2011**, *59*, 2035−2045.

(25) Kilner, J. A. Fast Oxygen Transport in Acceptor Doped Oxides. *Solid State Ionics* **2000**, *129*, 13−23.

(26) Minervini, L.; Zacate, M. O.; Grimes, R. W. Defect Cluster Formation in M_2O_3-Doped CeO_2. *Solid State Ionics* **1999**, *116*, 339−349.

(27) Liu, X.; Zhou, K.; Wang, L.; Wang, B.; Li, Y. Oxygen Vacancy Clusters Promoting Reducibility and Activity of Ceria Nanorods. *J. Am. Chem. Soc.* **2009**, *131*, 3140−3141.

(28) Shim, J. H.; Chao, C.-C.; Huang, H.; Prinz, F. B. Atomic Layer Deposition of Yttria-Stabilized Zirconia for Solid Oxide Fuel Cells. *Chem. Mater.* **2007**, *19*, 3850−3854.

(29) Horlait, D.; Claparède, L.; Clavier, N.; Szenknect, S.; Dacheux, N.; Ravaux, J.; Podor, R. Stability and Structural Evolution of CeIV1−xLnIIIxO2−x/2 Solid Solutions: A Coupled μ-Raman/XRD Approach. *Inorg. Chem.* **2011**, *50*, 7150−7161.

(30) Sanna, S.; Esposito, V.; Pergolesi, D.; Orsini, A.; Tebano, A.; Licoccia, S.; Balestrino, G.; Traversa, E. Fabrication and Electro-

DOI: 10.1021/acsami.6b03909
ACS Appl. Mater. Interfaces 2016, 8, 14613−14621

chemical Properties of Epitaxial Samarium-Doped Ceria Films on $SrTiO_3$-Buffered MgO Substrates. *Adv. Funct. Mater.* **2009**, *19*, 1713−1719.
(31) Rushton, M. J. D.; Chroneos, A. Impact of Uniaxial Strain and Doping on Oxygen Diffusion in CeO_2. *Sci. Rep.* **2014**, *4*, 6068−6073.
(32) Zha, S.; Xia, C.; Meng, G. Effect of Gd (Sm) Doping on Properties of Ceria Electrolyte for Solid Oxide Fuel Cells. *J. Power Sources* **2003**, *115*, 44−48.
(33) Omar, S.; Wachsman, E. D.; Jones, J. L.; Nino, J. C. Crystal Structure−Ionic Conductivity Relationships in Doped Ceria Systems. *J. Am. Ceram. Soc.* **2009**, *92*, 2674−2681.
(34) Taniguchi, T.; Watanabe, T.; Sugiyama, N.; Subramani, A. K.; Wagata, H.; Matsushita, N.; Yoshimura, M. Identifying Defects in Ceria-Based Nanocrystals by UV Resonance Raman Spectroscopy. *J. Phys. Chem. C* **2009**, *113*, 19789−19793.
(35) Korobko, R.; Chen, C.-T.; Kim, S.; Cohen, S. R.; Wachtel, E.; Yavo, N.; Lubomirsky, I. Influence of Gd Content on the Room Temperature Mechanical Properties of Gd-Doped Ceria. *Scr. Mater.* **2012**, *66*, 155−158.
(36) Rupp, J. L. M.; Scherrer, B.; Gauckler, L. J. Engineering Disorder in Precipitation-Based Nano-Scaled Metal Oxide Thin Films. *Phys. Chem. Chem. Phys.* **2010**, *12*, 11114−11124.
(37) McBride, J. R.; Hass, K. C.; Poindexter, B. D.; Weber, W. H. Raman and X-Ray Studies of $Ce_{1-x}RE_xO_{2-y}$, where RE = La, Pr, Nd, Eu, Gd, and Tb. *J. Appl. Phys.* **1994**, *76*, 2435−2441.
(38) Rupp, J. L. M.; Fabbri, E.; Marrocchelli, D.; Han, J.-W.; Chen, D.; Traversa, E.; Tuller, H. L.; Yildiz, B. Scalable Oxygen-Ion Transport Kinetics in Metal-Oxide Films: Impact of Thermally Induced Lattice Compaction in Acceptor Doped Ceria Films. *Adv. Funct. Mater.* **2014**, *24*, 1562−1574.
(39) Nakajima, A.; Yoshihara, A.; Ishigame, M. Defect-Induced Raman Spectra in Doped CeO_2. *Phys. Rev. B: Condens. Matter Mater. Phys.* **1994**, *50*, 13297−13307.
(40) Pikalova, E. Y.; Murashkina, A. A.; Maragou, V. I.; Demin, A. K.; Strekalovsky, V. N.; Tsiakaras, P. E. CeO_2 Based Materials Doped with Lanthanides for Applications in Intermediate Temperature Electrochemical Devices. *Int. J. Hydrogen Energy* **2011**, *36*, 6175−6183.
(41) Kumar, A.; Jaiswal, A.; Sanbui, M.; Omar, S. Scandia Stabilized Zirconia-Ceria Solid Electrolyte (xSc1CeSZ, 5< x< 11) for IT-SOFCs: Structure and Conductivity Studies. *Scr. Mater.* **2016**, *121*, 10−13.
(42) Avila-Paredes, H. J.; Choi, K.; Chen, C.-T; Kim, S. Dopant-Concentration Dependence of Grain-Boundary Conductivity in Ceria: A Space-Charge Analysis. *J. Mater. Chem.* **2009**, *19*, 4837−4842.
(43) Giannici, F.; Gregori, G.; Aliotta, C.; Longo, A.; Maier, J.; Martorana, A. Structure and Oxide Ion Conductivity: Local Order, Defect Interactions and Grain Boundary Effects in Acceptor-Doped Ceria. *Chem. Mater.* **2014**, *26*, 5994−6006.
(44) Baertsch, C. D.; Jensen, K. F.; Hertz, J. L.; Tuller, H. L.; Vengallatore, S. T.; Spearing, S. M.; Schmidt, M. A. Fabrication and Structural Characterization of Self-Supporting Electrolyte Membranes for a Micro Solid-Oxide Fuel Cell. *J. Mater. Res.* **2004**, *19*, 2604.
(45) Kumar, A.; Ciucci, F.; Morozovska, A. N.; Kalinin, S. V.; Jesse, S. Measuring Oxygen Reduction/Evolution Reactions on the Nanoscale. *Nat. Chem.* **2011**, *3*, 707−713.
(46) Kumar, A.; Jesse, S.; Morozovska, A. N.; Eliseev, E.; Tebano, A.; Yang, N.; Kalinin, S. V. Variable Temperature Electrochemical Strain Microscopy of Sm-Doped Ceria. *Nanotechnology* **2013**, *24*, 145401−145411.
(47) Yang, S. M.; Lee, S.; Jian, J.; Zhang, W.; Lu, P.; Jia, Q.; Wang, H.; Noh, T. W.; Kalinin, S. V.; MacManus-Driscoll, J. L. Strongly Enhanced Oxygen Ion Transport Through Samarium-Doped CeO_2 Nanopillars in Nanocomposite Films. *Nat. Commun.* **2015**, *6*, 8588.
(48) Doria, S.; Yang, N.; Kumar, A.; Jesse, S.; Tebano, A.; Aruta, C.; Di Bartolomeo, E.; Arruda, T. M.; Kalinin, S. V.; Licoccia, S.; Balestrino, G. Nanoscale Mapping of Oxygen Vacancy Kinetics in Nanocrystalline Samarium Doped Ceria Thin Films. *Appl. Phys. Lett.* **2013**, *103*, 171605−171608.
(49) Kumar, A.; Ovchinnikov, O. S.; Funakubo, H.; Jesse, S.; Kalinin, S. V. Real-Space Mapping of Dynamic Phenomena During Hysteresis Loop Measurements: Dynamic Switching Spectroscopy Piezoresponse Force Microscopy. *Appl. Phys. Lett.* **2011**, *98*, 202903−202905.
(50) Balke, N.; Jesse, S.; Kim, Y.; Adamczyk, L.; Ivanov, I. N.; Dudney, N. J.; Kalinin, S. V. Decoupling Electrochemical Reaction and Diffusion Processes in Ionically-Conductive Solids on the Nanometer Scale. *ACS Nano* **2010**, *4*, 7349−7357.
(51) Younis, A.; Chu, D.; Li, S. Evidence of Filamentary Switching in Oxide-Based Memory Devices Via Weak Programming and Retention Failure Analysis. *Sci. Rep.* **2015**, *5*, 13599.
(52) Kubicek, M.; Schmitt, R.; Messerschmitt, F.; Rupp, J. L. M. Uncovering Two Competing Switching Mechanisms for Epitaxial and Ultra-Thin Strontium Titanate-Based Resistive Switching Bits. *ACS Nano* **2015**, *9*, 10737−10748.

DOI: 10.1021/acsami.6b03909
ACS Appl. Mater. Interfaces 2016, 8, 14613−14621